


Article

# Physical and Chemical Properties Characterization of 3D-Printed Substrates Loaded with Copper-Nickel Nanowires

Ely Dannier V-Niño <sup>1,2,\*</sup> , Quentin Lonne <sup>3</sup>, Andrés Díaz Lantada <sup>4</sup>, Enrique Mejía-Ospino <sup>5</sup>, Hugo Armando Estupiñán Durán <sup>6</sup>, Rafael Cabanzo Hernández <sup>5</sup>, Gustavo Ramírez-Caballero <sup>5</sup> and José Luis Endrino <sup>1,7,\*</sup>

<sup>1</sup> BCMaterials, Basque Center for Materials, Applications and Nanostructures, UPV/EHU Science Park, 48940 Leioa, Spain

<sup>2</sup> Materials Science and Technology Research Group, Foundation of Researchers in Science and Technology of Materials, 680003 Bucaramanga, Colombia

<sup>3</sup> School of Aerospace, Transport and Manufacturing, Cranfield University, Bedfordshire MK43 0AL, UK; quentin.lonne@gmail.com

<sup>4</sup> Departamento de Ingeniería Mecánica, Universidad Politécnica de Madrid, 28006 Madrid, Spain; adiaz@etsii.upm.es

<sup>5</sup> Escuelas de Química, Física e Ingeniería Química, Universidad Industrial de Santander, 680002 Bucaramanga, Colombia; emejia@uis.edu.co (E.M.-O.); rcabanzo@uis.edu.co (R.C.H.); gusramca@uis.edu.co (G.R.-C.)

<sup>6</sup> Departamento de Materiales y Minerales, Universidad Nacional de Colombia, 050034 Medellín, Colombia; haestupinand@unal.edu.co

<sup>7</sup> IKERBASQUE, Basque Foundation for Science, 48013 Bilbao, Spain

\* Correspondence: deydannv@gmail.com (E.D.V.-N.); jose.endrino@bcmaterials.net (J.L.E.); Tel.: +34-94-465-1115 (E.D.V.-N. & J.L.E.)

Received: 9 July 2020; Accepted: 11 November 2020; Published: 13 November 2020



**Abstract:** This study deals with the laser stereolithography manufacturing feasibility of copper-nickel nanowire-loaded photosensitive resins. The addition of nanowires resulted in a novel resin suitable for additive manufacturing technologies based on layer-by-layer photopolymerization. The pure and nanowire-loaded resin samples were 3D printed in a similar way. Their morphological, mechanical, thermal, and chemical properties were characterized. X-ray computed tomography revealed that 0.06 vol % of the composite resin was filled with nanowires forming randomly distributed aggregates. The increase of 57% in the storage modulus and 50% in the hardness when loading the resin with nanowire was attributed to the load transfer. Moreover, the decrease in the glass transition temperature from 57.9 °C to 52.8 °C in the polymeric matrix with nanowires evidenced a decrease in the cross-linking density, leading to a higher mobility of the polymer chains during glass transition. Consequently, this research demonstrates the successful dispersion and use of copper-nickel nanowires as a reinforcement material in a commercial resin for laser stereolithography.

**Keywords:** nanofillers; bulk-functionalization; photopolymer resin; additive manufacturing; stereolithography

## 1. Introduction

Additive manufacturing (AM) technologies, often employed for rapid prototyping (RP), directly manufacture complex three-dimensional (3D) objects layer-by-layer using the information of computer-aided design (CAD) files. Polymeric, metallic, ceramic, and even composite materials can be processed, employing a wide range of technologies, among which vat photopolymerization

stands out due to the degree of precision and throughput achieved [1–3]. Vat photopolymerization technologies, including laser stereolithography (SLA) and digital light processing (DLP), work with a vat of photopolymerizable resin. They use the power of a laser or a light projected through a digital mask to selectively activate the polymerization of the resin in the vat, layer by layer. SLA, a laser which usually works in the ultraviolet range, is used for precisely defining the contours and infill of the polymeric layers. Both bottom-up and top-down systems exist, depending on the movement of the 3D printing bed inside the vat. The top-down equipment offers an excellent process stability, while the bottom-up set-ups stand out for their design simplicity. Sometimes however, the latter present some limitations related to the lack of adhesion of the 3D-printed part with the printing bed [1–3].

SLA is a 3D printing technique that can produce complex 3D structures easily, rapidly, and precisely; the SLA technique allows the production of a wide range of shapes and components and is considered as a method of reference in rapid RP [2,4–7]. It is already used to manufacture microelectromechanical systems (MEMSs) and microfluidic devices [5,6,8–11], and loading the photopolymerizable resin matrix with functional fillers opens the possibility of new composite materials and devices with tailored properties [12–15]. Several studies already present the development of functional composites with improved performance related to the manufacturing of flexible component materials [16–18]. Besides this, both the surface and bulk functionalization of the essential elements may lead to final devices with enhanced properties and innovative functionalities [7–15,19,20].

This study presents the evaluation of the physicochemical properties of substrates printed by SLA using a photosensitive resin with dispersed copper-nickel nanowires (CuNi NWs) as reinforcing agents. Additionally, the methods and materials used in the design and manufacture of the selected specimens are described. Hence, the analysis and discussion of the results obtained provide useful information regarding the potential benefits of the present approach.

## 2. Experimental Details

### 2.1. Materials and Methods

The base material used to manufacture the specimens was the commercial photoreactive resin “Clear FLGPCL 02” (Form 1+, Formlabs, Somerville, MA, USA) [10,11,15,19,21], which is a mixture of methacrylic acids esters (methacrylate oligomers and monomers) and photoinitiators, according to the manufacturer’s datasheet.

The CuNi NWs for mass-functionalization were provided by the Surface Engineering and Nanotechnology Institute (Cranfield University, Bedford, UK) in a solution of isopropyl alcohol (IPA). The total mass of this IPA/NW ink was 9.38 g, including 0.16 g of CuNi NWs. The process used to synthesize pure Cu NWs has been previously reported by some of the authors [22]. Typically, copper chloride dihydrate and nickel acetate hexahydrate were mixed and heated at 190 °C in oleylamine. The nickel ions  $\text{Ni}^{2+}$  were reduced by the oleylamine in  $\text{Ni}^0$ , and, subsequently,  $\text{Ni}^0$  reduced the  $\text{Cu}^{2+}$  ions in  $\text{Cu}^0$  in a galvanic reaction. The nickel only had a catalytic role, and pure Cu NWs were obtained. In this study, however, the temperature of the synthesis was increased to above 200 °C to enhance the reduction kinetics of the catalytic nickel, and, hence, some nickel was incorporated into the NWs (~ 20 mol%). Consequently, CuNi alloy NWs were obtained instead of pure Cu NWs [22]; they were washed and stored in IPA to form an IPA/NW ink.

The IPA/NW ink was mixed with an incline of 30° at high speed in the MPC 004ST vacuum casting machine (SLM Solutions, Lübeck, Germany) for 30 min, and then with a magnetic stirrer bar for 90 min to 1000 rpm in the stirring hot plates model SPA 1020B (Thermolyne Corporation, Dubuque, IA, USA); Figure 1a shows the pure resin while Figure 1b shows the CuNi NW-loaded resin.

Cylindrical substrates with a diameter of 21.3 mm and a thickness of 3 mm were designed using the FreeCAD v0.16 software and the CAD designs were exported to Standard Tessellation Language/StereoLithography (STL) format, which is a standard file format for additive manufacturing technologies and 3D printers [19]. The fabrication of the substrates with and without CuNi NWs was

then carried out using the SLA technique with a Formlabs Form 1+ printer [7,15,19,21]. It followed a bottom-up approach, starting with the printing bed completely immersed in the resin vat, and used a laser to photopolymerize the resin layer-by-layer from below, through the transparent bottom of the vat [3,15,19]. Three substrates of pure resin (Figure 1c) and 3 substrates of CuNi NW-loaded resin (Figure 1d) were SLA-printed, with a resolution of 100  $\mu\text{m}$  per layer and a total printing time of 34 min [19].

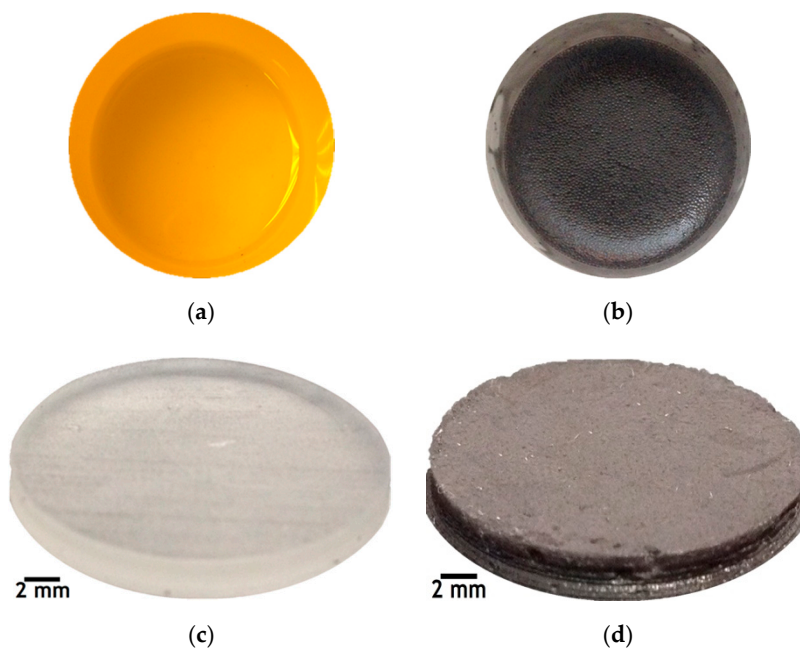


**Figure 1.** Pictures of (a) the pure resin, (b) the resin mixed with the IPA/NW ink, the SLA-printed (c) pure resin substrate, and (d) the CuNi NW-loaded substrate.

## 2.2. Characterization Techniques

The surface morphology and elemental composition of the SLA-printed, CuNi NW-loaded substrates were analyzed by scanning electron microscopy (SEM) in the microscope thermionic emission ZEISS EVO MA10 (ZEISS, Oberkochen, Germany); from the images obtained by secondary electrons and backscattered electrons, the elements' identification and distribution on the image were acquired by electrons and energy dispersive spectroscopy (EDS) with the detector Oxford X-act (Oxford Instruments, Abingdon, UK) coupled with SEM. Additionally, the 3D distribution of the CuNi NWs in the polymeric matrix was performed with a computed tomography (CT) system XT H 160 CT SCAN (Nikon, Tokyo, Japan); it used an energy beam of 150 kV and 50  $\mu\text{A}$ , and the working distance between the specimen and the detector was set to optimize the phase contrast between the NWs and the polymeric matrix. The exposure time was 500 ms, where four frames (each one of 540 projections) were collected by radiography. Moreover, the voxel size was fixed at 10  $\mu\text{m}$ , which was adequate to image the selected region.

The mechanical properties were characterized by nano-indentation testing with a Berkovich-type indenter, a force of 10 mN, and a 10 s creep in the IBIS-Authority nano-indentation system (Fischer-Cripps Laboratories Pty Limited, Sydney, Australia). The storage moduli ( $E'$ ) and hardness ( $H$ ) were obtained from 30 indentations separated from each other by 30  $\mu\text{m}$ .

A dynamic mechanical analysis (DMA) was carried out on a Q800 analyzer (TA Instruments Inc., New Castle, Delaware, USA) to characterize the viscoelastic behavior of the substrates. During the sweep tests, the sample was clamped at both ends; a frequency of 1 Hz, a ramp rate of 5  $^{\circ}\text{C}/\text{min}$ , a temperature range of 30  $^{\circ}\text{C}$  to 90  $^{\circ}\text{C}$ , and a force of 1 N were used. The instrument was completely calibrated in accordance with the procedures of TA Instruments. In these tests,  $E'$  is the storage

modulus—i.e., the elastic component that measures the energy stored during one oscillation cycle—and is related to the sample stiffness;  $E''$  is the loss modulus—i.e., the viscous component that measures the mechanical energy dissipated through molecular motion in an oscillation cycle; and  $\tan \delta$  is the relationship between the elastic and inelastic components (phase lag referred to as loss tangent) that arises from any of the several molecular-level loss processes such as entanglement, slip, or friction between the monomers. Furthermore,  $\tan \delta$  has higher values for amorphous polymers and lower values for more crystalline polymers [19,23].

The thermal behavior of the specimens manufactured in the pure and CuNi NW-loaded resin was characterized by differential scanning calorimetry (DSC) and thermogravimetric analysis (TGA) using an STA 449 F5 Jupiter system (NETZSCH, Selb, Germany) operated under a nitrogen atmosphere. Samples were analyzed between 30 and 600 °C with a heating rate of 10°C/min to determine their glass transition temperatures and crystallographic properties.

The Raman spectroscopy characterization of the substrates manufactured in pure and CuNi NW-loaded resin was performed to determine the vibration bands of the species on their surface. The Raman spectra were acquired using the Horiba Scientific confocal spectrometer LabRam HR (HORIBA, Kyoto, Japan) equipped with a 532 nm laser and a 100× microscope objective; all the Raman spectra were obtained with a 15 mW laser power and a grating of 600g/mm (slit aperture) for 8 s acquisition times. The LabSpec 6 software Horiba Scientific (HORIBA, Kyoto, Japan) was used for Raman spectra acquisition and analysis, where each sample was scanned in the range of 25–4000  $\text{cm}^{-1}$ .

The Fourier-transformed infrared (FTIR) spectra on substrates that were SLA-printed in pure and CuNi NW-loaded resin were obtained by the attenuated total reflection (ATR) technique in the Nicolet iS50 Spectrometer (Thermo Fisher Scientific, Waltham, MA, USA). The spectra were analyzed in terms of transmittance in the wavenumber range of 400–4000  $\text{cm}^{-1}$ , using a resolution of 4  $\text{cm}^{-1}$  and an optical velocity of 0.1581cm/s; this analysis was used to determine the absorption bands of the organic functional groups on the surface of the substrates.

X-ray diffraction (XRD) patterns of the substrates in pure and CuNi NWs-loaded resin were acquired in the powder diffractometer Bruker model D8 Advance with DaVinci geometry under the following conditions: a 40 kV voltage, a 0.6 mm divergence gap, a LynxEye linear detector, a 0.02035° step, an acquisition time of 0.6 s per step, and a range of 3.5–70°. The qualitative analysis of the phases was performed through the comparison of the experimental XRD patterns with the database PDF-2 (2014) of the International Centre for Diffraction Data (ICDD).

### 3. Results and Discussion

#### 3.1. Cost Considerations

The manufacturing time of a cylindrical specimen, with or without CuNi NWs, was approximately 340 s—i.e., 11 s per layer of 3.6  $\text{cm}^2$ . In the present case, considering only the chemicals used for the synthesis and washing of the NWs, the cost for the CuNi NWs reaches 0.45 €/mg, whereas it is 0.14 €/mL for the pure resin. Hence, the manufacturing cost of a functional device containing CuNi NWs greatly depends on their content. In this study, with a load of 0.36% w/w, the cost of each specimen of pure resin was approximately 0.14 €, while it was 1.65 € for those manufactured with CuNi NWs.

#### 3.2. Morphology

The micrograph in Figure 2a in secondary electron mode shows the topographical image of the surface of an SLA-printed, CuNi NW-loaded specimen, with yellow arrows pointing at CuNi NW aggregates embedded in the photopolymerized resin. These NW aggregates are even better highlighted in backscattered electron mode (Figure 2b) thanks to the large atomic number difference between Cu/Ni and the main elements in the resin, carbon (C) and oxygen (O) (the heavier the atomic number,

the brighter the image). Hence, SEM observations evidence the presence of CuNi NW aggregates randomly dispersed in the polymeric matrix, which explains the absence of percolation.

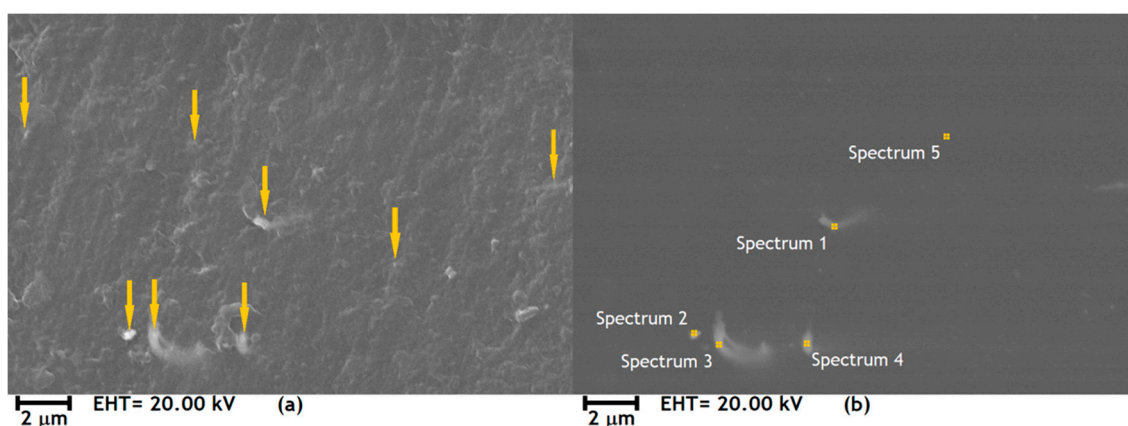


**Figure 2.** SEM images on the surface of a CuNi NW-loaded substrate; (a) secondary electron micrograph, with yellow arrows indicating the position of the CuNi NW aggregates; and (b) backscattered electron micrograph, which shows the regions analyzed by EDS.

EDS was also used on the surface the CuNi NW-loaded substrate to analyze its elemental composition. The results are summarized in Table 1 and the locations of the EDS analyses are shown on Figure 2b, with spectra 1 to 4 corresponding to CuNi NW aggregates and spectrum 5 to pure resin. In all the spectra, Cu and Ni correspond to the NWs, and C and O correspond to the resin. Cu and Ni are not detected in the region of spectrum 5 (pure resin), which means that the NWs were not degraded and dissolved in the polymeric matrix during the manufacturing process (at least not significantly, the EDS detection limit being 0.1 wt.%).

**Table 1.** Atomic contents (in %) of the elements detected by EDS on the surface of a CuNi NW-loaded substrate.

Element	Spectrum (At %)				
	1	2	3	4	5
C k	83.6	85.5	84.3	84.0	87.3
O k	14.9	12.7	14.2	9.1	12.7
Cu k	1.0	1.4	1.0	5.7	-
Ni k	0.5	0.4	0.5	1.2	-

In Figure 3, the X-ray tomogram shows the 3D distribution of the CuNi NW aggregates in the photopolymerized resin matrix after SLA printing. The brightness of an X-ray tomogram depends on the atomic number of the elements constituting the sample, with a higher atomic number giving a brighter image [19,24–26]. Given the large atomic number difference between Cu/Ni and the main elements constituting the resin (C and O), it was possible to map a random 3D distribution of the CuNi NWs in the polymeric matrix. In the analyzed region of 50.6 mm<sup>3</sup>, the detected volume of CuNi NWs approximately corresponds to 0.06 vol.%. Moreover, Figure 3 confirms the SEM results (Figure 2) at a 3D level. The CuNi NWs form randomly dispersed aggregates in the polymeric matrix, preventing their percolation.

To conclude on morphological considerations, due to randomly dispersed aggregates without percolation, the CuNi NWs are expected to influence the thermo-mechanical properties [19,27,28] of the polymer matrix but not its electrical properties [19,29]. The aggregation phenomenon is likely due to the resin's high viscosity and the presence of polar groups on the polymeric chains [19,24–26]. In any case, a homogeneous dispersion of the NWs in the polymeric matrix without aggregates is

the key to reach achieve percolation with a minimal NW content. Moreover, this would lead to an optimized manufacturability (closer to the pure resin), a lower cost (see Section 3.1), and homogeneous properties in the 3D-printed composites [19].

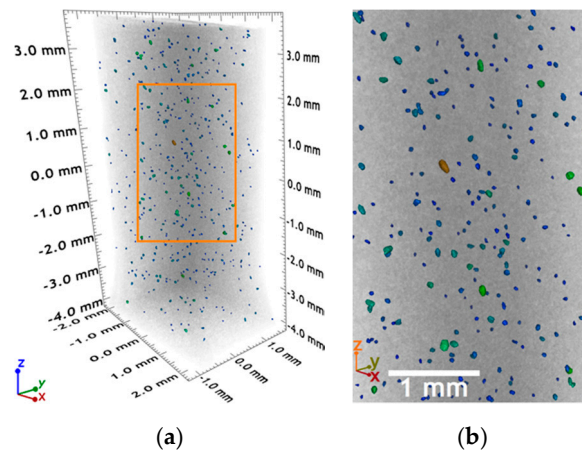


**Figure 3.** (a) 3D rendering of the CuNi NW-loaded resin and (b) magnification of the region in the red rectangle in (a).

### 3.3. Mechanical and Thermal Analysis

Mappings of the mechanical properties  $E'$  (Figure 4a,b) and  $H$  (Figure 4c,d) were obtained from nanoindentation tests on the surfaces of pure and CuNi NW-loaded, SLA-printed substrates. The total surface area of the mappings is  $120 \times 150 \mu\text{m}^2$ , and the variations in the  $E'$  and  $H$  values are represented by color scales, with a darker color corresponding to a higher value. The advantage such mappings is to directly and visually assess local variations in the mechanical properties. Moreover, the average values extracted from these mappings can be representative of the entire specimens if the studied areas are large enough (Figure 5) [19,30,31].

In the case of the pure resin, the variations in  $E'$  and  $H$  are likely due to the SLA process itself (surface roughness, surface defects, etc.). In the case of the CuNi NW-loaded substrate, two other parameters influence  $E'$  and  $H$ : the NW aggregate concentration and the quality of the polymeric matrix/NW aggregate bonding. Since there is a significant increase in  $E'$  (57%) and  $H$  (50%) when loading the resin with NWs (Figure 5), it is assumed that the influence of the SLA process on  $E'$  and  $H$  can be neglected compared to the influence of the NWs. Moreover, as the dispersion of the NW aggregates seems random and rather uniform (Figure 2), it can be assumed that the main factor driving the variation in  $E'$  and  $H$  is the matrix/NW bonding.

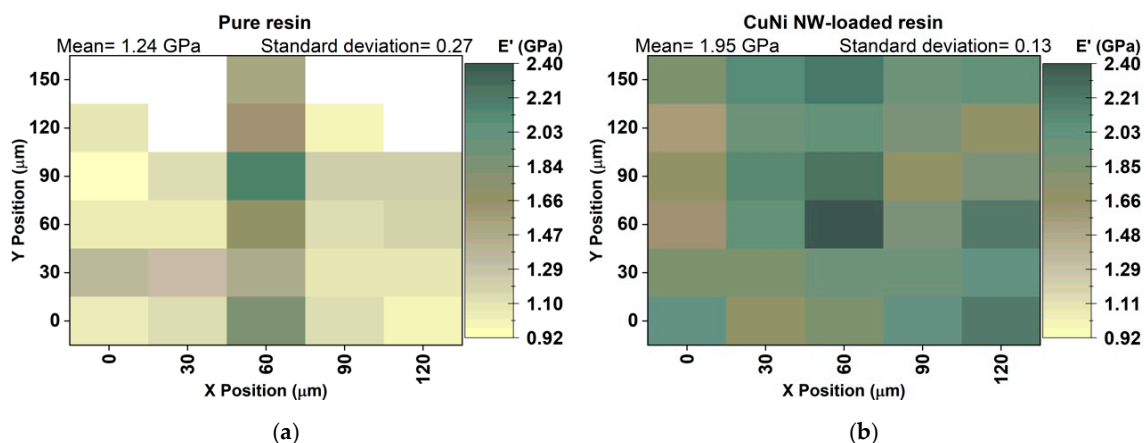


**Figure 4.** Cont.

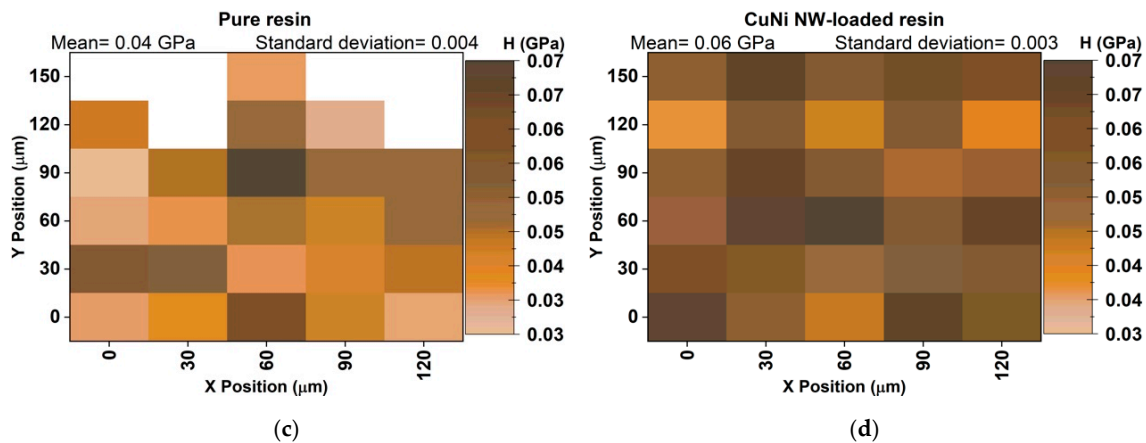


**Figure 4.** Mappings of the mechanical properties  $E'$  (a,b) and  $H$  (c,d), obtained from the nanoindentation tests on the surface of the pure and CuNi NW-loaded resin substrates, respectively. A total surface area of  $120 \times 150 \mu\text{m}^2$  was analyzed on each substrate.

The CuNi NW aggregates seem to act as hardeners inside the matrix, and a higher matrix/NW aggregate bonding quality provides a higher load transfer from the NWs to the matrix and, hence, higher mechanical properties ( $E'$  and  $H$ ). On the contrary, some NW aggregates may be only slightly infiltrated by the polymer and constitute local defects with low mechanical properties. Obtaining well-dispersed fillers in a polymeric matrix (instead of aggregates) is consequently a major focus in many studies, as this is the key to obtain an optimized matrix/filler bonding, a maximal load transfer, and enhanced properties [19,30–34].

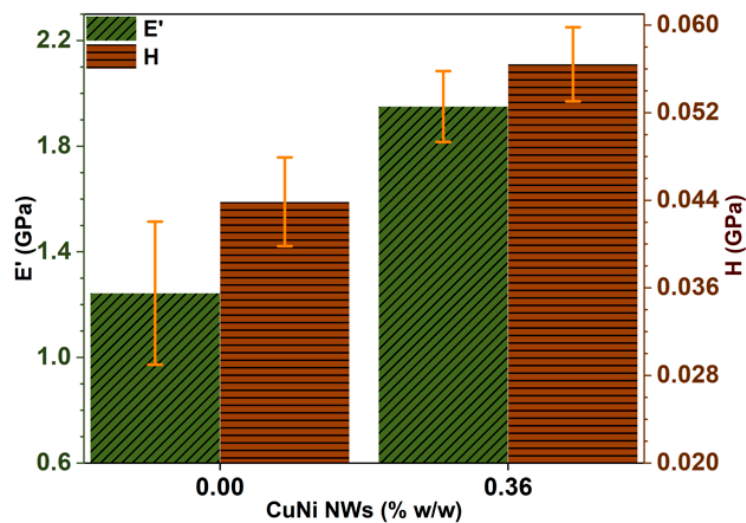


**Figure 5.** Average values of  $E'$  (green) and  $H$  (brown) for the pure and CuNi NW-loaded substrates, corresponding to the mappings in Figure 4.

Figure 6 presents the evolution of  $E'$  and  $\tan \delta$  as a function of the temperature, between  $30^\circ\text{C}$  and  $90^\circ\text{C}$ , for pure and CuNi NW-loaded substrates. Figure 6a shows that  $E'$  decreases for both substrates when the temperature increases between  $30^\circ\text{C}$  and  $60^\circ\text{C}$ , highlighting a glass transition region. Moreover,  $E'$  is significantly higher for the pure resin than for the CuNi NW-loaded one in this temperature range, and the maximum  $E'$  values, measured at  $30^\circ\text{C}$ , are 600.2 and 300.1 MPa for the pure and CuNi NW-loaded substrates, respectively. Furthermore, factors such as the reaction degree and the crosslinking density mainly influence the value of  $E'$ . The glass transition process is thereby confirmed, suggesting that the behavior of the material with and without CuNi NWs can be evaluated through the rheological properties.

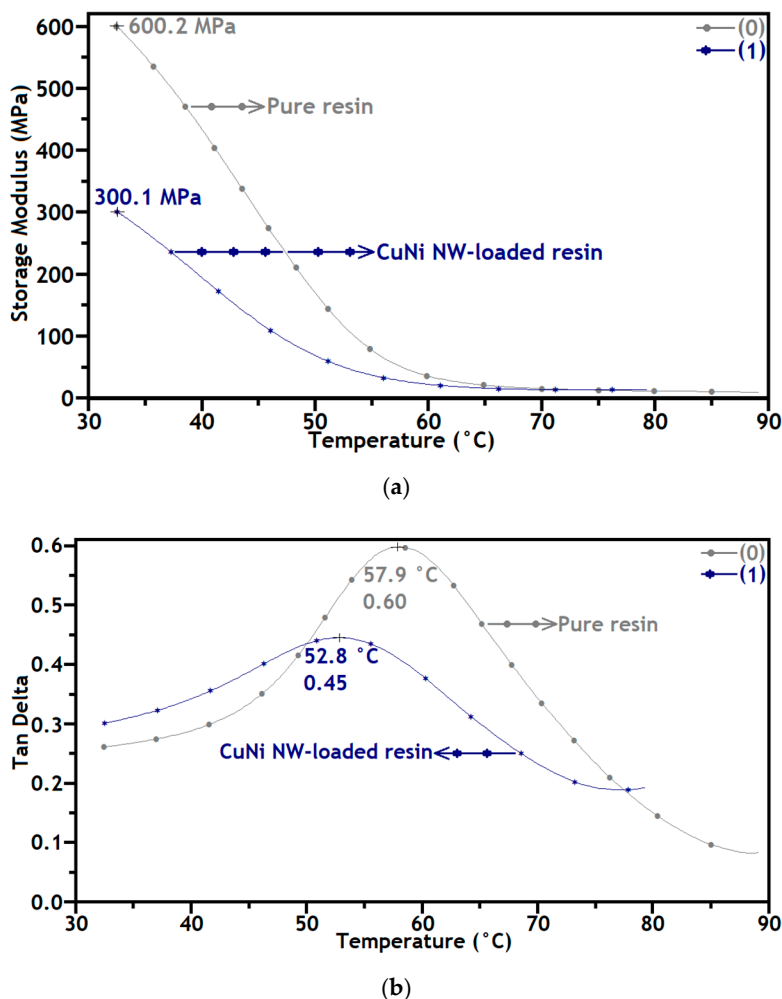


**Figure 6.** DMA curves of the pure (0) and CuNi NW-loaded (1) substrates for (a)  $E'$  and (b)  $\tan \delta$ , as a function of temperature.

In Figure 6b, the maximum values of  $\tan \delta$  correspond to the glass transition temperatures ( $T_g$ ), 57.9 and 52.8 °C, of the pure and CuNi NW-loaded resins, respectively (see also Table 2) [35]. Loading the polymeric matrix with CuNi NWs lowers the  $T_g$ , which could be due to a poor resin matrix/NW aggregate bonding. Indeed, a lack of chemical interaction between the resin and the CuNi NWs can decrease the crosslinking density and lead to a higher mobility of the polymeric chains in the composite, resulting in a lower  $T_g$  [19,35–39]; this is confirmed by a sharper peak around the maximum value of  $\tan \delta$  for the pure resin, which indicates a more ordered structure due to a higher crosslinking density.

**Table 2.** Values determined from the DMA, DSC, and TGA analysis.

CuNi NWs Content	Transition and Degradation Temperatures (°C)	
	$T_g$ – DMA	$T_g$ – DSC
0.00% w/w	57.9	60.8
0.36% w/w	52.8	51.6

The addition of CuNi NWs highly influenced the molecular dynamics in the polymeric matrix, which resulted in a reduction in  $T_g$  and  $E'$  [35,36]. The DMA results show a more elastic behavior of the CuNi NW-loaded substrate compared to the pure resin one, suggesting the enhanced stiffness of the material.



The DSC curves in Figure 7a show a broad glass transition region between 32 and 135 °C for the pure substrate ( $T_g = 60.8$  °C) and between 31 and 97 °C for the CuNi NW-loaded one ( $T_g = 51.6$  °C) [35]; thus, the glass transition region and  $T_g$  slightly decreased when loading the resin with CuNi NWs, and the results were in agreement with the DMA analysis (see Table 2). Moreover, the crystallization temperature, corresponding to the maximum of the first exothermal peak, is lower for the CuNi NW-loaded composite (ca. 121 °C) than for the pure resin (ca. 160 °C).

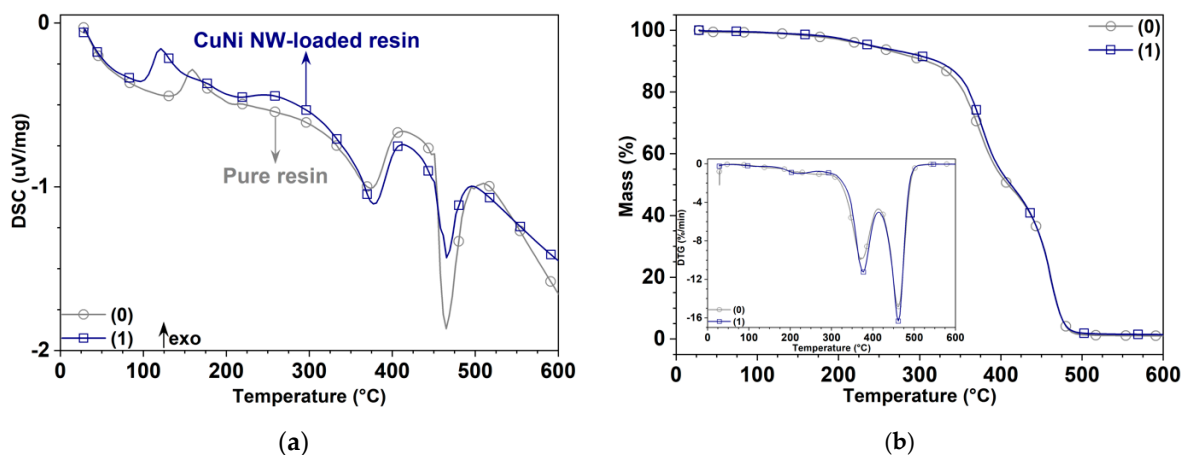


**Figure 7.** Thermal analysis of the pure (0) and CuNi NW-loaded (1) substrates by (a) DSC, (b) TGA, and DTGA (insert) as a function of the temperature.

The thermal stability of the samples was investigated by TGA between 32 and 600 °C under an  $N_2$  atmosphere (Figure 7b); the slight mass loss between 80 and 100 °C may be due to the evaporation of adsorbed IPA in the resin, although most of it should have evaporated during the manufacturing process. The weight loss between 100 and 300 °C was mainly attributed to the evaporation of physisorbed and chemisorbed water [35]. Finally, most of the thermal degradation of the samples occurring between 300 and 500 °C was likely due to the evaporation of organic species from the resin (e.g., methacrylic acid and ester) [19,35–39]. Moreover, as the TGA curves are similar for both materials, it can be assumed that the NWs were not significantly degraded during the heating ramp and that the weight loss was mainly driven by the polymeric matrix degradation.

A mechanical and thermal analysis of pure and CuNi NW-loaded, SLA-printed samples was carried out. It seems that the addition of NWs to the polymeric matrix increased the mechanical surface properties (Figures 4 and 5) thanks to a load transfer phenomenon. However, it decreased the thermomechanical bulk properties (Figures 6 and 7) due to interfacial defects in the composite material (weak NW/matrix bonding).

### 3.4. Spectroscopic Characterization

The Raman spectra obtained on the substrates manufactured in the “Clear FLGPCL 02” pure resin and CuNi NW-loaded resin at 0.36%  $w/w$  are presented in Figure 8, where Cu and Ni present vibrational modes at very low frequencies (phonon frequencies,  $\sim 10$   $cm^{-1}$ ).

The spectrum of Figure 8 from the surface of the pure resin substrate reveals three intense Raman peaks at 1441 (strong), 2928, and 2948  $cm^{-1}$  (very intense) that correspond to the C-H bond vibrations. Consequently, the medium and weak peaks at 1560 and 1590  $cm^{-1}$  are attributed to the C-N-H and C-NO<sub>2</sub> bond vibrations, respectively. The peaks at 595  $cm^{-1}$  (medium) and 1608  $cm^{-1}$  (weak) correspond to the C-C and C = C bond vibrations, respectively. The medium peaks at 1632 and 1712  $cm^{-1}$  refer to the C=O symmetric and antisymmetric bond vibrations, and the one at 1396  $cm^{-1}$  to the CH<sub>3</sub> asymmetric bond stretching vibration. The band between 785 and 980  $cm^{-1}$  corresponds to the C-O-C bond vibrations, the one between 1000 and 1160  $cm^{-1}$  to the C-O-C bond asymmetric stretching vibrations, and the one between 1300 and 1380  $cm^{-1}$  to the C-CH<sub>3</sub> bond

vibrations. Additionally, the weak peaks at 2650–2810 and 3050–3500  $\text{cm}^{-1}$  are attributed to the O-C-H and O-H bond vibrations, respectively.

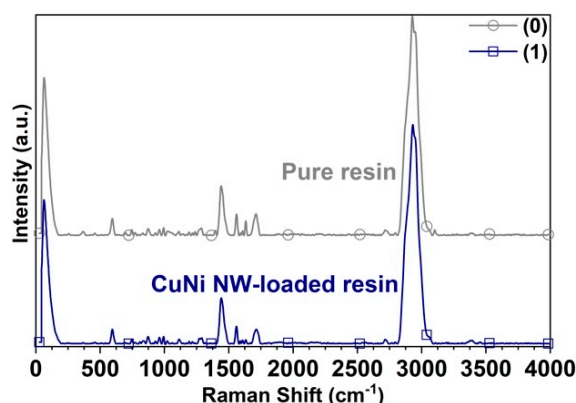


**Figure 8.** Raman spectra acquired on the substrates printed with (0) pure resin and (1) CuNi NW-loaded resin.

Raman spectroscopy reveals the surface interaction between organic materials and metallic nanostructures through surface-enhanced Raman scattering. Figure 8 shows similar Raman spectra from the pure resin and CuNi NW-loaded resins; however, it is possible to observe intensification in vibrational signals corresponding to the C-H (2928  $\text{cm}^{-1}$ –2948  $\text{cm}^{-1}$ ) and O-H (3050  $\text{cm}^{-1}$ –3500  $\text{cm}^{-1}$ ) vibrational modes [19,35,40–42]. This is evidence of the surface interaction between the polymeric resin and CuNi NWs through the C-H and O-H functional groups. Furthermore, metallic structures such as Cu and Ni do not present vibrational frequencies (phonon frequencies) in the range of wavenumbers observed in this study. Thus, this surface interaction can be responsible for the difference in  $T_g$  before and after doping. Additionally, these studies allowed us to identify differences in the degree of crystallinity due to the influence of the doping agents.

The characteristic Raman spectrum of the photopolymer resin matrix shows a main peak with a maximum intensity of 1780 counts in the pure resin and 1834 counts in the one with nanowires; the peak also exhibits a wavelength shift from 2926 to 2930  $\text{cm}^{-1}$  with the addition of the nanofillers. The increase in the intensification of the peak with nanowires corresponds to the energy difference in the vibrational state of the methacrylate molecule, which is related both to the level of polymer structuring and to electromagnetic intensification due to the plasmonic effect produced by the presence of the nanowires in the polymer matrix. On the other hand, the displacement of the peak to a greater wavelength indicates a change in the electronic dispersion of the molecules on the surface of the polymer, which implies evident structural changes in the molecular bonds and a greater crosslinking that corroborate the thermo-mechanical results shown.

In order to determine if the increasing aggregate of nickel-copper nanowires affects the chemical structure of the photopolymer resin, FTIR measurements were conducted to determine whether alterations occur in the main chemical groups of the polymer. The results show no alterations attributable to the presence of the CuNi NWs in the concentration studied 0.36%  $w/w$ ; therefore, the polymer adequately fulfills its support function as a nanomaterial (Figure 9).

Figure 9 presents the FT-IR spectrum of the substrates manufactured in pure resin and CuNi NW-loaded resin, where there are distinct absorption bands from 1150 to 1250  $\text{cm}^{-1}$ , which can be attributed to the C-O-C stretching vibrations. The two bands at 1386 and 748  $\text{cm}^{-1}$  can be attributed to the  $\alpha$ -methyl group vibrations. Moreover, the bands at 865, 1297, 1367, and 1405  $\text{cm}^{-1}$  can be attributed to the C-C, O-CH<sub>2</sub>, C-H, and C-OH stretching vibrations, respectively. The band at 1700  $\text{cm}^{-1}$  indicates the presence of the ester group C=O stretching vibrations. The band at 1451  $\text{cm}^{-1}$  can be attributed to the bending vibrations of the C-H bonds of the -CH<sub>3</sub> groups. The three bands at 2952, 2932, and 2862  $\text{cm}^{-1}$  can be assigned to the C-H bond stretching vibrations. Furthermore, there are two weak

absorption bands at  $3375$  and  $1637\text{ cm}^{-1}$ , which can be attributed to the  $-\text{OH}$  group stretching and bending vibrations, respectively. Notwithstanding this, there are no appreciable differences between the FTIR spectra of the pure resin and the CuNi NW-loaded resin because the resin does not form any covalent bond with this type of nano-additives; additionally, the nanowires do not add new functional groups, which can be observed with infrared. According to the above discussions, it can be concluded that the photoreactive polymer resin is composed of a macromolecular methacrylic acid (MAA) and a methyl methacrylate (MMA) mixture [19,35,39,43,44].

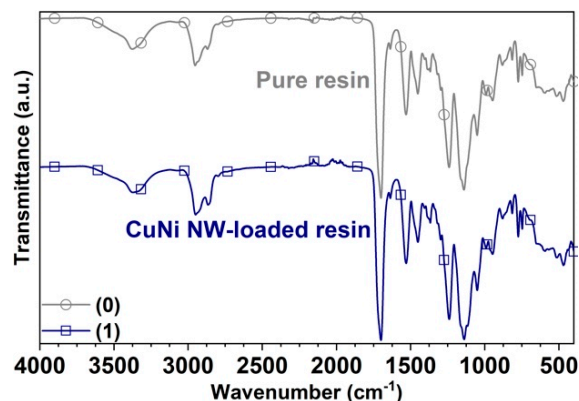


**Figure 9.** FTIR spectra acquired on the substrates printed with (0) pure resin and (1) CuNi NW-loaded resin.

The semiquantitative analysis of the phases found in the specimens was performed using the Rietveld method. The percentages determined correspond to the polycrystalline phases without considering the percentage of amorphous material. The XRD patterns of Figure 10 prove that the CuNi NWs contained in some of the substrates manufactured by 3D printing have a face-centered cubic structure (in agreement with the database PDF-02 of the ICDD). Additionally, the contents of 59.8% copper and 40.2% nickel were evaluated in a semiquantitative analysis. No diffraction peak was observed on the XRD pattern of the “Clear FLGPCL 02” resin without nanowires because it is amorphous.

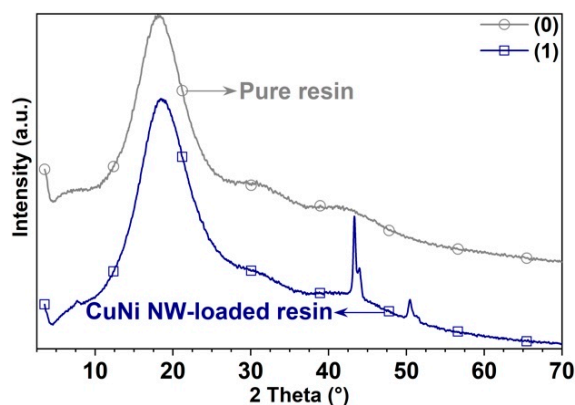


**Figure 10.** XRD patterns acquired on the substrates printed with (0) pure resin and (1) CuNi NW-loaded resin.

The spectroscopy analysis clearly indicates some structural changes, which might be due to an intermolecular transformation; thus, the incorporation of the nanowires affects the polymerization process, decreasing the scattering and crosslinking points. The results obtained allowed us to know the morphologic, mechanical, thermal, and spectrometric behavior of photopolymers resins, with and without CuNi NWs, used for 3D printing by the SLA technique. Notwithstanding this, the effect of CuNi NWs was not as predominant as expected. The reason for this is that many parameters

involved in the manufacturing process, such as the concentration and dispersion of the CuNi NWs, the specimens' size, and the polymerizing process interaction between the laser of the printer and the CuNi NWs, caused the physicochemical properties to not improve significantly with regard to the pure resin. Moreover, the highlight of this research was that specimens of cylindrical geometry reinforced with CuNi NWs were successfully manufactured by 3D printing through the SLA technique.

#### 4. Conclusions

This paper presents the manufacturing of new polymeric resin substrates functionalized with CuNi NWs by the SLA technique. Copper-nickel alloy nanowires were successfully dispersed in the "Clear FLGPCL 02" resin, which is a typical resin used in 3D printing by the stereolithography technique. Besides the functionalization improvements, the manufacturability of three-dimensional objects by the SLA technique (3D printing) using a mass-functionalized photopolymer with CuNi NWs is demonstrated. Moreover, a homogeneous 3D distribution of the CuNi NWs inside the polymeric matrix was achieved, and the presence of the nanowires correlated with the modification of the mechanical and thermal properties of the resin. It was also demonstrated that the addition of CuNi NWs reduces the crosslinking density and leads to the higher mobility of the polymeric chains during the glass transition. Furthermore, both the melting and degradation temperatures remained unchanged below 600 °C, which was expected as Cu and Ni have higher melting points (1085 and 1455 °C, respectively). This study underscores the possible use of the SLA technique, in combination with functional nanomaterials, in the fabrication of new precision devices and for wearable electronics such as advanced transducers, flexible sensors, circuit/devices using self-assembly approaches, robotic parts, microfluidic devices, and microelectromechanical systems.

**Author Contributions:** E.D.V.-N. and A.D.L. conceived, designed, and performed the experiments; analyzed the data; and wrote the paper. Q.L. supported with the synthesis of the nanowires. E.M.-O., R.C.H., and G.R.-C. worked on X-ray diffraction (XRD) and Fourier-transform infrared (FTIR) spectroscopy, dynamic mechanical analysis (DMA), differential scanning calorimetry (DSC), and thermogravimetric analysis (TGA). H.A.E.D. worked on the Raman spectroscopy and scanning electron microscopy/energy dispersive X-ray spectroscopy (SEM/EDS). J.L.E. managed and coordinated the overall research. All the authors contributed to the discussion of the results. All authors have read and agreed to the published version of the manuscript.

**Funding:** This work was partially financed by the Colombian agency Colciencias through doctoral scholarship 617. This work was partly funded by the Spanish MINECO Retos project SUSANA (PID2019-108103RB-C31). The support from project Frontiers2020 funded by the Basque Government under the ELKARTEK call is also gratefully acknowledged.

**Acknowledgments:** The authors express their gratitude to the Laboratorio de Difracción de Rayos X, Laboratorio de Espectroscopia Atómica y Molecular, Centro de Investigación Científica y Tecnológica en Materiales y Nanociencia, Parque Tecnológico Guatimar, Universidad Industrial de Santander.

**Conflicts of Interest:** The authors declare no conflict of interest.

#### References

1. Ford, S.; Despeisse, M. Additive manufacturing and sustainability: An exploratory study of the advantages and challenges. *J. Clean. Prod.* **2016**, *137*, 1573–1587. [[CrossRef](#)]
2. Jacobs, P.F. *Stereolithography and Other RP&M Technologies: From Rapid Prototyping to Rapid Tooling*; Society of Manufacturing Engineers: Dearborn, MI, USA, 1996.
3. Bhushan, B.; Caspers, M. An overview of additive manufacturing (3D printing) for microfabrication. *Microsyst. Technol.* **2017**, *23*, 1117–1124. [[CrossRef](#)]
4. Brennan-Craddock, J.; Brackett, D.; Wildman, R.; Hague, R. The design of impact absorbing structures for additive manufacture. *J. Phys. Conf. Ser.* **2012**, *382*, 1–7. [[CrossRef](#)]
5. Ho, K.S.; Bradley, R.J.; Billson, D.R.; Hutchins, D.A. Micro-stereolithography as a transducer design method. *Ultrasonics* **2008**, *48*, 1–5. [[CrossRef](#)]
6. Maruo, S.; Ikuta, K. Submicron stereolithography for the production of freely movable mechanisms by using single-photon polymerization. *Sens. Actuators A Phys.* **2002**, *100*, 70–76. [[CrossRef](#)]

7. Wang, J.; Goyanes, A.; Gaisford, S.; Basit, A.W. Stereolithographic (SLA) 3D printing of oral modified-release dosage forms. *Int. J. Pharm.* **2016**, *503*, 207–212. [[CrossRef](#)]
8. Zhang, X.; Jiang, X.N.; Sun, C. Micro-stereolithography for MEMS. In Proceedings of the 1998 ASME International Mechanical Engineering Congress and Exposition, Anaheim, CA, USA, 15–20 November 1998.
9. Wicker, R.B.; Medina, F.; Ranade, A.; Palmer, J.A. Embedded micro-channel fabrication using lines can stereolithography. *Assem. Autom.* **2005**, *25*, 316–329. [[CrossRef](#)]
10. Díaz Lantada, A.; Rebollo, M. Towards low-cost effective and homogeneous thermal activation of shape memory polymers. *Materials* **2013**, *6*, 5447–5465. [[CrossRef](#)]
11. Díaz Lantada, A.; de Blas Romero, A.; Tanarro, E.C. Micro-vascular shape-memory polymer actuators with complex geometries obtained by laser stereolithography. *Smart Mater. Struct.* **2016**, *25*, 1–10. [[CrossRef](#)]
12. de Leon, A.C.; Chen, Q.; Palaganas, N.B.; Palaganas, J.O.; Manapat, J.; Advincula, R.C. High performance polymer nanocomposites for additive manufacturing applications. *React. Funct. Polym.* **2016**, *103*, 141–155. [[CrossRef](#)]
13. Kumar, S.; Hofmann, M.; Steinmann, B.; Foster, E.J.; Weder, C. Reinforcement of stereolithographic resins for rapid prototyping with cellulose nanocrystals. *ACS Appl. Mater. Interfaces* **2012**, *4*, 5399–5407. [[CrossRef](#)] [[PubMed](#)]
14. Sandoval, J.H.; Wicker, R.B. Functionalizing stereolithography resins: Effects of dispersed multi-walled carbon, nanotubes on physical properties. *Rapid Prototyp. J.* **2006**, *12*, 292–303. [[CrossRef](#)]
15. V-Niño, E.D.; Endrino-Armenteros, J.L.; Estupiñán-Duran, H.A.; Pérez-Gutiérrez, B.; Díaz Lantada, A. Caracterización microscópica de texturas superficiales fabricadas aditivamente mediante estereolitografía laser. *Respuestas* **2016**, *21*, 37–47. [[CrossRef](#)]
16. Corrado, A.; Polini, W. Measurement of high flexibility components in composite material by touch probe and force sensing resistors. *J. Manuf. Process.* **2019**, *45*, 520–531. [[CrossRef](#)]
17. Li, H.; Shin, K.; Henkelman, G. Effects of ensembles, ligand, and strain on adsorbate binding to alloy surfaces. *J. Chem. Phys.* **2018**, *149*, 1–8. [[CrossRef](#)] [[PubMed](#)]
18. Wang, M.; Xie, R.; Chen, Y.; Pu, X.; Jiang, W.; Yao, L. A novel mesoporous zeolite-activated carbon composite as an effective adsorbent for removal of ammonia-nitrogen and methylene blue from aqueous solution. *Bioresour. Technol.* **2018**, *268*, 726–732. [[CrossRef](#)]
19. V-Niño, E.D.; Díaz Lantada, A.; Lonne, Q.; Estupiñán Durán, H.A.; Mejía-Ospino, E.; Ramírez-Caballero, G.; Endrino, J.L. Manufacturing of polymeric substrates with copper nanofillers through laser stereolithography technique. *Polymers* **2018**, *10*, 1325. [[CrossRef](#)]
20. Kirihera, S.; Miyamoto, Y.; Takenaga, K.; Wada Takeda, M.; Kajiyama, K. Fabrication of electromagnetic crystals with a complete diamond structure by stereolithography. *Solid State Commun.* **2002**, *121*, 435–439. [[CrossRef](#)]
21. Inverardi, N.; Pandini, S.; Bignotti, F.; Scalet, G.; Marconi, S.; Auricchio, F. Temperature-memory effect in 3D printed photopolymers with broad glass transition. *AIP Conf. Proc.* **2018**, *1981*, 1–10.
22. Lonne, Q.; Endrino, J.L.; Huang, Z. UV treatment of flexible copper nanowire mesh films for transparent conductor applications. *Nanoscale Res. Lett.* **2017**, *12*, 1–8. [[CrossRef](#)]
23. Cohen, S.R.; Kalfon-Cohen, E. Dynamic nano-indentation by instrumented nano-indentation and force microscopy: A comparative review. *Beilstein J. Nanotechnol.* **2013**, *4*, 815–833. [[CrossRef](#)] [[PubMed](#)]
24. Cnudde, V.; Jacobs, P.J.S. Monitoring of weathering and conservation of building materials through non-destructive X-ray computed microtomography. *Environ. Geol.* **2004**, *46*, 477–485. [[CrossRef](#)]
25. Hong, G.; Choi, S. Rapid self-sealing of cracks in cementitious materials incorporating superabsorbent polymers. *Constr. Build. Mater.* **2017**, *143*, 366–375. [[CrossRef](#)]
26. Garcea, S.C.; Sinclair, I.; Spearing, S.M.; Withers, P.J. Mapping fibre failure in situ in carbon fibre reinforced polymers by fast synchrotron X-ray computed tomography. *Compos. Sci. Technol.* **2017**, *149*, 81–89. [[CrossRef](#)]
27. Crosby, A.J.; Lee, J.-Y. Polymer nanocomposites: The “nano” effect on mechanical properties. *Polym. Rev.* **2007**, *47*, 217–229. [[CrossRef](#)]
28. Bansal, A.; Yang, H.; Li, C.; Benicewicz, B.C.; Kumar, S.K.; Schadler, L.S. Controlling the thermomechanical properties of polymer nanocomposites by tailoring the polymer-particle interface. *J. Polym. Sci. Part B Polym. Phys.* **2006**, *44*, 2944–2950. [[CrossRef](#)]
29. Ye, S.; Rathmell, A.R.; Chen, Z.; Stewart, I.E.; Wiley, B.J. Metal nanowire networks: The next generation of transparent conductors. *Adv. Mater.* **2014**, *26*, 6670–6687. [[CrossRef](#)]

30. Chakraborty, A.K.; Plyhm, T.; Barbezat, M.; Necola, A.; Terrasi, G.P. Carbon nanotube (CNT)–epoxy nanocomposites: A systematic investigation of CNT dispersion. *J. Nanopart. Res.* **2011**, *13*, 6493–6506. [[CrossRef](#)]
31. Gayle, A.J.; Cook, R.F. Mapping viscoelastic and plastic properties of polymers and polymer-nanotube composites using instrumented indentation. *J. Mater. Res.* **2016**, *31*, 2347–2360. [[CrossRef](#)]
32. Sandler, J.; Shaffer, M.S.P.; Prasse, T.; Bauhofer, W.; Schulte, K.; Windle, A.H. Development of a dispersion process for carbon nanotubes in an epoxy matrix and the resulting electrical properties. *Polymer* **1999**, *40*, 5967–5971. [[CrossRef](#)]
33. Xie, X.L.; Mai, Y.W.; Zhou, X.P. Dispersion and alignment of carbon nanotubes in polymer matrix: A review. *Mater. Sci. Eng. R* **2005**, *49*, 89–112. [[CrossRef](#)]
34. Ma, P.C.; Siddiqui, N.A.; Marom, G.; Kim, J.K. Dispersion and functionalization of carbon nanotubes for polymer-based nanocomposites: A review. *Compos. Part A* **2010**, *41*, 1345–1367. [[CrossRef](#)]
35. V.-Niño, E.D. *Systematic Research of Physicochemical Properties of Functional Photopolymers for Additive Manufacturing*; Universidad Politécnica de Madrid: Madrid, Spain, 2019.
36. Vadukumpully, S.; Paul, J.; Mahanta, N.; Valiyaveetil, S. Flexible conductive graphene/poly(vinyl chloride) composite thin films with high mechanical strength and thermal stability. *Carbon* **2011**, *49*, 198–205. [[CrossRef](#)]
37. Jyotishkumar, P.; Pionteck, J.; Hassler, R.; George, S.M.; Cvelbar, U.; Thomas, S. Studies on stress relaxation and thermomechanical properties of Poly(acrylonitrile-butadiene-styrene) modified epoxy-amine systems. *Ind. Eng. Chem. Res.* **2011**, *50*, 4432–4440.
38. Wei, X.; Li, D.; Jiang, W.; Gu, Z.; Wang, X.; Zhang, Z.; Sun, Z. 3D printable graphene composite. *Sci. Rep.* **2015**, *5*, 1–7. [[CrossRef](#)]
39. Doganay, D.; Coskun, S.; Kaynak, C.; Unalan, H.E. Electrical, mechanical and thermal properties of aligned silver nanowire/poly(lactide) nanocomposite films. *Compos. Part B* **2016**, *99*, 288–296. [[CrossRef](#)]
40. Hua, M.Z.; Feng, S.; Wang, S.; Lu, X. Rapid detection and quantification of 2,4-dichlorophenoxyacetic acid in milk using molecularly imprinted polymers–surface-enhanced Raman spectroscopy. *Food Chem.* **2018**, *258*, 254–259. [[CrossRef](#)]
41. Sessa, C.; Weiss, R.; Niessner, R.; Ivleva, N.P.; Stege, H. Towards a surface enhanced Raman scattering (SERS) spectra database for synthetic organic colourants in cultural heritage. The effect of using different metal substrates on the spectra. *Microchem. J.* **2018**, *138*, 209–225. [[CrossRef](#)]
42. Garcia-Rico, E.; Alvarez-Puebla, R.A.; Guerrini, L. Direct surface-enhanced Raman scattering (SERS) spectroscopy of nucleic acids: From fundamental studies to real-life applications. *Chem. Soc. Rev.* **2018**, *47*, 4909–4923. [[CrossRef](#)]
43. Zhao, T.; Li, X.; Yu, R.; Zhang, Y.; Yang, X.; Zhao, X.; Wang, L.; Huang, W. Silicone–epoxy-based hybrid photopolymers for 3D printing. *Macromol. Chem. Phys.* **2018**, *219*, 1–10. [[CrossRef](#)]
44. Weng, Z.; Zhou, Y.; Lin, W.; Senthil, T.; Wu, L. Structure-property relationship of nano enhanced stereolithography resin for desktop SLA 3D printer. *Compos. Part A* **2016**, *88*, 234–242. [[CrossRef](#)]

**Publisher’s Note:** MDPI stays neutral with regard to jurisdictional claims in published maps and institutional affiliations.



© 2020 by the authors. Licensee MDPI, Basel, Switzerland. This article is an open access article distributed under the terms and conditions of the Creative Commons Attribution (CC BY) license (<http://creativecommons.org/licenses/by/4.0/>).